Pre-print

Resentini, A., Andò, S., Garzanti, E., Malusà, M.G., Pastore, G., Vermeesch, P., Chanvry, E., Dall'Asta, M. (2020) Zircon as a provenance tracer: Coupling Raman spectroscopy and U-Pb geochronology in source-to-sink studies. Chemical Geology, 555, 119828.

https://doi.org/ 10.1016/j.chemgeo.2020.119828

https://doi.org/10.1016/j.chemgeo.2020.119828

ZIRCON AS A PROVENANCE TRACER: COUPLING RAMAN SPECTROSCOPY AND U-Pb GEOCHRONOLOGY IN SOURCE-TO-SINK STUDIES

Alberto Resentini [a,*], Sergio Andò [a], Eduardo Garzanti [a], Marco G. Malusà [a], Guido Pastore [a], Pieter Vermeesch [b], Emmanuelle Chanvry [c,d], Massimo Dall'Asta [d]

* Corresponding Author

[a] Laboratory for Provenance Studies, Department of Earth and Environmental Sciences, University of Milano-Bicocca, 20126 Milano, Italy

[b] London Geochronology Centre, Department of Earth Sciences, University College London, London, WC1E 6BT, UK

[c] IC2MP CNRS-UMR 7285, Université de Poitiers, Poitiers, France

[d] TOTAL E&P, CSTJF, Pau, France

ABSTRACT

U-Pb zircon geochronology is one of the most widely used techniques in sedimentary provenance analysis. Unfortunately, the ability of this method to identify sediment sources is often degraded by sediment recycling and mixing of detritus from different source rocks sharing similar age signatures. These processes create non-unique zircon U-Pb age signatures and thereby obscure the provenance signal. We here address this problem by combining detrital zircon U-Pb geochronology with Raman spectroscopy. The position and width of the Raman signal in zircon scales with its degree of metamictization, which in turn is sensitive to temperature. Thus, combined U-Pb + Raman datasets encode information about the crystallisation history of detrital zircons as well as their thermal history. Using three borehole samples from Mozambique as part of a source-to-sink study of interest for hydrocarbon exploration, we show that zircon populations with similar U-Pb age distributions can exhibit different Raman signatures. The joint U-Pb + Raman analysis allowed us to identify three different annealing trends, which were linked to specific thermal events. Thus we were able to differentiate a dominant Pan-African U-Pb age peak into several sub-populations and highlight the major effect of Karoo tectono-magmatic events. In our case study, we used Raman

also as a means to systematically identify all zircon grains in heavy-mineral mounts, resulting in considerable time savings. Raman spectroscopy is a non-destructive and cost-effective method that is easily integrated in the zircon U-Pb dating workflow to augment the resolution power of detrital zircon U-Pb geochronology.

Key words: Provenance analysis; U-Pb zircon geochronology; Raman Spectroscopy; Zircon metamictization; Hydrocarbon exploration; Mozambique.

Highlights:

- Raman spectroscopy supplements U-Pb geochronological analysis of detrital zircon
- Thermal overprints revealed by the diverse metamict states of zircon crystals
- New approach allows discrimination of source rocks with same age of crustal growth

1. Introduction

In an era of great improvement of data-acquisition techniques, zircon geochronology is playing a key role in the renewed interest and success of detrital studies (e.g., Zimmermann et al., 2018). Large sets of reliable U-Pb zircon ages are now rapidly obtained at a reasonable cost and with continuously enhanced efficiency, thus allowing provenance analysis to enter a new era of "big data" (Vermeesch and Garzanti, 2015).

Zircon, a common accessory component in magmatic and metamorphic rocks, is particularly valuable in the study of sand and sandstone owing to its durability among detrital minerals (Velbel, 1999; Fedo et al., 2003). In source-to-sink studies, zircon U-Pb data are widely used as a "barcode" fingerprint to be compared with the age signature of the potential sediment sources (Condie et al., 2009; Gehrels, 2011). The reliability of provenance inferences based on zircon-age fingerprinting, however, is strictly dependent on the existence of source-rock domains characterized by well-defined U-Pb ages. If the potential sources show broad and partially overlapping age spectra, then zircon ages loose much of their discrimination power. Nonetheless, the amount of information that can be extracted from zircon grains is not limited to U-Pb ages, but includes geochemical tracers (e.g., REE or other trace elements; Hoskin and Ireland, 2000), isotopic tracers (e.g., hafnium and oxygen; Kemp et al., 2006), fission tracks (Hurford and Carter, 1991), U-Th/He dating (Farley, 2002), and zircon typology (Pupin, 1980). Because of the high content of uranium and thorium (up to 4000 ppm), zircon is on the one hand the ideal target for several dating techniques but on the other hand its crystalline structure is prone to progressive amorphization, owing to accumulation of structural defects induced by recoiling nuclei produced during α-emission events (Ewing et al., 1987; Weber et al., 1994). The metamictization process induces a physical transformation of zircon crystals with reduction in density and birefringence, decrease in the elastic moduli and Poisson's ratio, darkening of colour, decrease in hardness, and increase in OH content (e.g., Holland and Gottfried, 1955; Chakoumakos et al., 1987). The transformation from crystalline to amorphous

zircon is a reversible process by subsequent heating, which may eventually lead to annealing and restoration of the crystalline structure (Geisler, 2002). The metamict state of zircon grains thus depends on both actinide content and thermal history (Ginster et al., 2019).

The degree of metamictization of zircons can be quantified by Raman spectroscopy (Nasdala et al., 1998, 2001; Zhang et al., 2000), which represents a potentially powerful tool to be applied in advanced provenance analysis. The treasure of information encrypted in the structure and chemical composition of zircon crystals can thus be profitably retrieved by combining classical U-Pb dating with the non-destructive Raman technique.

This article defines a protocol designed in a source-to-sink study of interest for hydrocarbon exploration in an area of southeastern Africa where Archean cratons and Proterozoic mobile belts have recorded different and complex thermal histories associated with a series of major magmatic events. As an example, we use here three core samples from the Cretaceous sedimentary succession of the Zambezi Delta in central Mozambique. By combining the Raman spectrum of each zircon grain with its U/Pb age, we could single out detrital subpopulations distinguished not only by their age but also by their thermal overprint. This new approach represents a promising step forward in zircon-based provenance analysis.

2. Radiation-induced damage and annealing of zircon lattice

Metamict substances were recognized by Brøgger (1896) as a new class of amorphous matter previously classified as “hyaline” or “porodine” (i.e., amorphous substances that were originally crystalline). Accumulation of damage to the crystal structure by the decay of radioactive actinides is considered the main cause of metamictization in U and Th-bearing minerals (e.g., zircon and monazite). Decay events produce α particles that move through the crystalline structure and create several thousand atomic displacements (Murakami et al., 1991).

Different stages of metamictization resulting from damage accumulation have been observed in zircon crystals. In ~570 Ma old natural zircons from Sri Lanka (Murakami et al., 1991), low radiation doses (<3 · 10^{15} α-events/mg) were observed to produce punctual defects and isolated distortions in the crystal lattice, whereas with higher doses (3-9 · 10^{15} α-events/mg) only distorted crystalline domains remained randomly distributed in an amorphous matrix. At highest doses (≥ 1 · 10^{16} α-events/mg), zircon becomes amorphous. While damage is being accumulated in the zircon lattice, the annealing process competes to restore crystallinity. When annealing rate exceeds the rate of damage accumulation, defects are progressively amended (Geisler, 2002).

The annealing process is strongly temperature dependent. Metamict zircon can be annealed to crystalline state by heating in furnaces for a few hours at ~900 °C (Zhang et al., 2000). Uncertainties arise when considering annealing over geological times. Metzger and Krogstad (1997) argued that metamict zircons are completely recovered under metamorphic conditions at 600-650 °C, whereas the annealing rate at surface temperature is virtually zero (Hurley and Fairbairn, 1953). Like damage accumulation, the annealing process proceeds step by step, depending on the initial degree of metamictization. Fully metamict amorphous zircon anneals only marginally (Murakami et al., 1991), whereas for partially metamict zircon two-to-three stages of progressive annealing are necessary (Zhang et al., 2000; Geisler, 2002). Although the evolution of the annealing process is controversial (Nasdala et al., 2001), this study is based on the widely accepted concept that damage recovery operates through successive steps and at different rates chiefly controlled by temperature and time.

2.1. Zircon metamict state determined by Raman spectroscopy

Together with X-ray diffraction, infrared spectroscopy, electron microprobe and TEM analysis, Raman spectroscopy has long been established as a suitable means to evaluate the degree of zircon metamictization (Nasdala et al., 1998, 2001). As radiation damage increases, because of variations

in bond length and angles, all main Raman peaks progressively broaden, decrease in intensity, and shift towards lower wavenumbers. Among the characteristic Raman peaks, the one related to the Si-O ν_3 stretching band is most sensitive to damage accumulation. Crystalline zircon displays the $\nu_3(SiO_4)$ Raman peak at ~1008 cm^{-1} with 5 cm^{-1} full width at half maximum (FWHM). In amorphous zircon, the same Raman peak occurs at < 955 cm^{-1} with FWHM > 30 cm^{-1}.

These main features of the $\nu_3(SiO_4)$ Raman peak allow distinction of three classes of zircons based on their metamict state (Zhang et al., 2000; Nasdala et al., 1998): a) crystalline-to-slightly-metamict zircon with peak at 1008–1000 cm^{-1} and FWHM 5-10 cm^{-1}; b) metamict zircons with peak at 1000-990 and FWHM 10-20 cm^{-1}; c) fully metamict zircons with peak at 990-955 and FWHM 20-30 cm^{-1} (Fig. 1). Because the final metamict state of zircon crystals depends on both accumulated radiation dose and thermal annealing, the relationship between the characteristics of the $\nu_3(SiO_4)$ Raman peak and the α-dose is generally complex. A linear relationship between the accumulated dose and the FWHM was obtained by Nasdala et al. (2001) for crystalline to moderately metamict zircons not involved in thermal events after crystallization (Fig. 1).

3. Geology of Southern Africa

The Archean core of southern Africa includes the Zimbabwe Craton, comprising a central terrane flanked by two distinct 2.7 Ga greenstone belts (Fig. 2). The central terrane includes 3.5-2.95 Ga gneisses and possibly older greenstone belts, non conformably overlain by 2.9-2.8 Ga volcanic rocks and conglomerates or by a SE-ward thickening 3.0-2.7 Ga sedimentary succession. The craton was stabilized between 2.7 and 2.6 Ga and eventually intruded by the Great Dyke swarm at 2575 Ma (Jelsma and Dirks, 2002). The craton grew progressively during the Paleoproterozoic and Mesoproterozoic (Jacobs et al., 2008), and was affected by intraplate magmatism at 1.4-1.35 Ga in the south, and next again at 1.1 Ga (Hanson et al., 2006).

Orogens formed during the Mesoproterozoic include the Irumide Belt, extending from central Zambia in the SW to northern Malawi in the NE, delimited by the largely undeformed basement of the Bangweulu block in the NW, and largely affected by the Neoproterozoic orogeny in the west and southwest. The Irumide Belt includes granitoid suites emplaced between 1.65 and 1.55 Ga, between 1.36 and 1.33 Ga only in the NE, and between 1.05 and 0.95 Ga, together with siliciclastic and minor carbonate rocks deposited around 1.85 Ga. The metamorphic grade increases from greenschist facies in the NW (1.02 Ga) to upper amphibolite facies in the SE (1.05 Ga; De Waele et al., 2006). The Choma–Kalomo block in southern Zambia is a distinct Mesoproterozoic domain also including granitoid intrusions and amphibolite-facies metasediments affected by a thermal event between 1020 and 980 Ma (Glynn et al., 2017).

The major Neoproterozoic Pan-African orogeny is represented by the Damara–Lufilian–Zambezi belt, which stretches from coastal Namibia in the west and across Botswana and southern Zambia to finally connect with the Mozambique Belt in the east (Goscombe et al., 2019). The Zambezi Belt contains a volcano-sedimentary succession deformed under amphibolite-facies conditions at 0.9-0.8 Ga (Hanson, 2003), whereas eclogite-facies metamorphism dated at 592 Ma constrains the timing of subduction with subsequent thrust emplacement dated as 550-530 Ma (Hargrove et al., 2003).

The several km-thick Karoo Supergroup, including upper Paleozoic glacial sediments, shales and volcaniclastic sandstones followed by quartzo-feldspatho-lithic fluvial sediments in the Triassic, was widely deposited across southern Africa (Johnson et al., 1996; Catuneanu et al., 2005). Karoo sedimentation was terminated by flood-basalt eruptions recorded at ~180 Ma (Svensen et al., 2012). Rifting and break-up of Gondwana finally led to opening of the Indian Ocean in the Early Cretaceous, an event associated with extensive volcanism in the Mozambique channel (König and Jokat, 2010). Inland, fluvial and lacustrine sediments were deposited in the Kalahari basin during the Cenozoic, reworked by eolian activity during Quaternary dry stages (Haddon and McCarthy, 2005).

3.1. Core stratigraphy

The studied core is located in the Zambezi Delta region of central Mozambique. The Lower Cretaceous succession includes over 1 km-thick mudrocks with interbedded fine-grained feldspatho-quartzo-lithic to medium-grained feldspatho-litho-quartzose sandstones (Lower Lupata Fm.; Salman and Abdula, 1995). Sandstones include monocrystalline quartz with rounded to subrounded outline and abraded overgrowths and felsic volcanic to subvolcanic grains locally containing quartz phenocrysts (sample NH45, age: Valanginian/Hauterivian). Above, the medium to coarse-grained feldspatho-litho-quartzose or litho-feldspatho-quartzose sandstones interbedded in the 652 m-thick Upper Lupata Formation are overlain by a medium-grained feldspatho-quartzo-lithic volcaniclastic sand containing microlitic and felsitic volcanic lithics, and, locally, a few aegirine grains (sample NH27, age: late Aptian/earlyAlbian). The overlying Sena Formation, 2688 m-thick, includes fine to coarse-grained sandstones ranging in composition from quartzo-feldspathic to feldspatho-quartzose (NH10, age: Cenomanian/Turonian). Granitoid rock fragments are common and garnet-bearing micaschist grains occur. Above, the 366 m-thick Upper Cretaceous to Oligocene succession includes fine to medium-grained litho-feldspatho-quartzose sandstones, followed by 219 m-thick, feldspar-rich feldspatho-quartzose to feldspatho-litho-quartzose sandstones of Miocene age.

4. Methods

Zircon grains from the three selected sand-sized samples NH45, NH27, and NH10 were concentrated using standard gravimetric and magnetic techniques. From an aliquot of the 15-500 μm size class obtained by wet sieving, dense minerals were separated in sodium polytungstate (ρ=2.90 g/cm^3) and recovered after partial freezing with liquid nitrogen. Zircons were concentrated with a Frantz isodynamic magnetic separator. The concentrate, obtained without any additional

separation either with denser liquids or by hand-picking to avoid selection bias, was poured on a standard glass slide, impregnated with araldite epoxy, and polished to expose the grain surfaces.

A complete photo-mosaic acquired for each slide using a motorized stage and camera was geo-referenced in a GIS environment using a previously defined Cartesian reference system. All grains were outlined by image-segmentation techniques. For each grain, the coordinates of its centroid were calculated, and the corresponding points analysed with a Renishaw InVia™ Raman spectrometer (laser 532 nm; 5 cycles of 0.5 s each; 20x magnification; laser power 30 mW on sample). After baseline correction, the collected spectra were classified based on a reference database, allowing the identification of all zircon grains together with their coordinates for further analyses. One of the advantages of such automated phase mapping (Vermeesch et al., 2017) is that all zircons are picked, including murky grains easily discarded by visual inspection.

For each Raman spectrum identified as zircon, the position and width of the diagnostic peaks at 202-235, 356, 438, 974, 1008 cm^{-1} (Dawson et al., 1971) were calculated using the peak-fitting algorithm designed for Matlab™ by Tom O'Haver (2020), which uses an unconstrained non-linear optimization algorithm to decompose the Raman spectrum into its component parts. A pseudo-Voigt shape was selected for peak fitting (Fig. 3). The precise position and full widths at half maximum (FWHM) of the $\nu_3(SiO_4)$ Raman peak located around 1008 cm^{-1} were recorded (Appendix Table A1).

U-Pb dating of the same zircon grains analysed by Raman spectroscopy was carried out at the London Geochronology Centre using an Agilent 7700x laser ablation-inductively coupled plasma-mass spectrometry (LA-ICP-MS) system, employing a NewWave NWR193 Excimer Laser operated at 10 Hz with a 20 μm spot size and ~ 2.5 J/cm^2 fluence. The laser spot was invariably placed in the middle of zircon grains in the same place analysed by Raman spectroscopy. The mass spectrometer data were converted to isotopic ratios using GLITTER 4.4.2 software (Griffin et al., 2008), employing Plešovice zircon (Sláma et al., 2008) as a primary age standard and GJ-1 (Jackson et al., 2004) as a secondary age standard. NIST SRM612 was used as a compositional standard for

the U and Th concentrations. We used $^{206}Pb/^{238}U$ and $^{207}Pb/^{206}Pb$ ages for zircons younger and older than 1100 Ma, respectively. No common Pb correction was applied. Grains with > +5/-15% age discordance were discarded.

For each dated grain, the alpha-decay dose was calculated according to Condon et al. (2015) assuming a concentration of $^{235}U \approx 1/137.818\ ^{238}U$:

(1) $$dose = 8\left[^{238}U\right]e^{(_{238U}\lambda\times age)-1} + 7\left[^{235}U\right]e^{(_{235U}\lambda\times age)-1} + 6\left[^{232}Th\right]e^{(_{232Th}\lambda\times age)-1}.$$

Geochemical and geochronological data, $\nu_3(SiO_4)$ Raman peak positions and widths, and the calculated alpha-decay dose for each zircon grain are provided in Appendix Table A1.

5. Results

The ICP-MS analysis of the studied zircon grains has revealed a rather uniform distribution in actinide concentration among the samples, with [^{238}U] ranging from 222 to 3485 ppm and [Th] from 73 and 2330 ppm (5th and 95th percentiles respectively; Appendix Table A1). The radiation dose calculated for each zircon grain based on *equation 1* ranges from ~2.5 · 10^{14} to ~ 1.5 · 10^{16} α-events/mg. Sample NH10 and NH27 display the same range of α-decay events/mg (from 2 · 10^{14} to 1.2 · 10^{16}), whereas a larger range is obtained for sample NH45 (from 4 · 10^{14} to 1.5 · 10^{16}), where the highest doses are found. The average doses are similar overall (10^{15}) but increase from sample NH10 (2.9 · 10^{15}) to samples NH27 and NH45 (~ 4 · 10^{15}). The two main age clusters recurring in the analysed samples are named for simplicity “Irumide” (0.9–1.1 Ga, Tonian to Stenian) and “Pan-African” (0.5–0.65 Ga, Cambrian to late Neoproterozoic).

5.1. U/Pb zircon ages

In the three selected samples, 90 to 160 zircon grains have been dated overall, but only grains with concordant age and for which the Raman spectrum allowed confident determination of the position and width of the $\nu_3(SiO_4)$ Raman peak were considered for further analysis (Fig. 4). The U-Pb age spectrum of detrital zircons from sample NH45 (n = 61) shows prominent Pan-African and Irumide peaks. The youngest ages form a Permian cluster (259-276 Ma, 7% of total ages), the oldest ages are Paleoproterozoic (1649-2066 Ma, 5% of total ages).

Detrital zircons in sample NH27 (n = 64) yielded clusters of Early Cretaceous (110-118 Ma, 14% of total ages), Pan-African (17% of total ages), Irumide (31% of total ages) and late Paleoproterozoic U-Pb ages (1676-2055 Ma, 16% of total ages). One Permian (265 Ma) and one Devonian age (380 Ma) were also obtained. The U-Pb age spectrum of detrital zircons from sample NH10 (n = 134) displays dominant Pan-African (42% of total ages) and Irumide peaks with one Early Cretaceous (128 Ma) and three Paleoproterozoic ages (1855-2146 Ma).

5.2. Raman analysis

From the three selected samples, 259 detrital zircons were analysed considering the position and width (full width at half maximum – FWHM) of the $\nu_3(SiO_4)$ Raman peak. The position varies between 994 and 1008 cm^{-1}, whereas FWHM varies between 5 and 24 cm^{-1}. Most analyzed zircon grains are crystalline (peak position > 1002 cm^{-1} and width < 10 cm^{-1}), whereas <25% of them show Raman characteristics typical of metamict grains. Fully metamict amorphous zircons with FWHM values > 30 cm^{-1} were not detected. Raman scattering results are uniformly distributed among the three samples irrespective of their stratigraphic position. In all samples, peak positions and FWMH values display inverse correlation (r -0.90 overall, ranging from -0.87 to -0.92) (Fig. 5) with mathematical relationship estimated as:

(2) $$\nu_3(SiO4)\text{peak position} = 1010 * e^{-0.0006209*\nu_3(SiO4)\text{FWHM}}.$$

Equation 2 allows us to use the peak position, which is more reproducible and easier to obtain than the commonly used FWHM value (e.g., Nasdala et al., 2001), as a proxy of zircon metamict state.

6. Discussion

6.1 Relationship between zircon age and metamict state

The accumulated radiation doses are strongly variable within each age population of zircon grains, because they depend not only on the time available for α-decay but also on actinide concentration, which varies over two orders of magnitude. Doses calculated for grains younger than 1.5 Ga cover the entire spectrum from $0.2 \cdot 10^{15}$ up to $1.2 \cdot 10^{16}$ α-events/mg, whereas higher doses characterize only grains older than 1.5 Ga, which never show values lower than $3.5 \cdot 10^{15}$ α-events/mg (Fig. 6A).

Because the position and width of the $\nu_3(SiO_4)$ Raman peak are strongly dependent on the metamictic state of zircon grains (and consequently on the accumulated damage by α decay), a correlation between age and Raman peak position (or width) is expected, with oldest zircons characterized by highest doses. However, low positions and large widths of the $\nu_3(SiO_4)$ Raman peaks are displayed only by zircons dated around 0.1, 0.6, and 1 Ga, whereas older zircons are invariably characterized by rather narrow peaks (Fig. 6B, 6C). The lack of old metamict zircon grains may have two explanations: a) strongly metamict zircons are prone to chemical dissolution (Ewing et al., 1982; Balan et al., 2001) and possibly also to mechanical breakdown during sediment transport owing to reduced hardness (Chakoumakos et al., 1987), and may thus be selectively lost during one or more sedimentary or metamorphic cycles (Malusà et al., 2013; Garzanti et al., 2019); b) strongly metamict zircons are characterized by such low and wide Raman peaks (fig. 1 in Zhang et al., 2000) that their identification becomes problematic. In any case, the high crystallinity of even

the oldest zircon grains testifies to the role played by subsequent thermal events that induced lattice annealing.

6.2 Relationship between radiation dose and Raman peak position

As shown in Fig. 7A, the relationship between the accumulated radiation dose and the position of the $\nu_3(SiO_4)$ Raman peak is complex. As the radiation dose increases, the $\nu_3(SiO_4)$ Raman peak of zircon grains unaffected by annealing processes would be expected to broaden and shift towards lower values (Fig. 1). However, the observed distribution fails to follow such a simple linear trend, and zircon grains that have experienced a wide range of α-decay damage accumulation display the same position of the Raman peak. Such an unexpected distribution is ascribed to different temperature-time histories of source rocks.

Based on the fact that annealing of the zircon lattice proceeds step-by-step, as shown by laboratory experiments (Murakami et al., 1991; Geisler, 2002), in our samples we identify three populations of zircon grains following different trends in the α-dose *vs*. $\nu_3(SiO_4)$-Raman-peak diagram (Fig. 7A). The slopes of such trends can be quantitatively defined by means of a frequency plot where the downshift of the Raman peak relative to 1008 cm^{-1} is related to the accumulated radiation dose (Fig. 7B).

Trend 1 (Fig. 7), with the steepest negative slope matches well the expected pattern for unannealed zircons (Fig. 1), whereas the other two trends indicate different temperature/time annealing paths. *Trend 2* (Fig. 7), with intermediate slope, indicates only partial annealing, whereas *trend 3*, with the gentlest slope, reflects a more extensive lattice recovery, which implies more recent annealing, higher-temperature conditions, or longer thermal overprint.

Considering the overall similarity of slopes calculated for the three samples separately (from -3 to -8 cm^{-1}/α-event mg^{-1} for *trend 1*, from -0.9 to -1.7 for *trend 2*, and from -0.1 to -0.4 for *trend 3*), we assumed that the source areas were affected by the same main thermal events. Data from all studied

zircons thus allow us to more robustly define three lines − all sharing an intercept 1008 cm^{-1} (crystalline zircon) − with slopes -5.5 for *trend 1*, -1.5 for *trend 2*, and -0.4 for *trend 3* (Fig. 7C, 7D, 7E). Each zircon grain was thus assigned to *trend 1*, *2*, or *3* based on the trend line found within the shortest Euclidean distance. By this procedure, in each sample between 21% and 39% of zircon grains were assigned to *trend 1* (crystalline zircons), 27-49% of grains to *trend 2* (partially annealed zircons), and 20-44% of grains to *trend 3* (extensively annealed zircons).

6.3 Relationship between zircon age and metamict state

By combining U-Pb ages with the metamict state of each zircon grain, the age populations of zircon grains identified in the three samples can be split into diverse subpopulations. The relative proportions of such subpopulations vary from sample to sample.

Sample NH10 shows three age groups (<0.7 Ga, 50%; 0.7-1.5 Ga, 48%; >1.5 Ga, 2%). In the young group, 54% of zircon grains are crystalline (*trend 1*), 37% are partially annealed (*trend 2*), and 9% are extensively annealed (*trend 3*). In the intermediate age group, 25% of grains are crystalline, 47% are partially annealed, and 28% extensively annealed. In the old group, all zircons appear to be extensively annealed.

Sample NH27 shows four age groups (<0.3 Ga, 16%; 0.3-0.7, 20%; 0.7-1.5 Ga, 53%; >1.5 Ga, 11%). In the youngest group, 90% of zircon grains are crystalline (*trend 1*), 10% are partially annealed (*trend 2*), and none is extensively annealed (*trend 3*). In the "Pan-African" age group, 23% of grains are crystalline, 31% are partially annealed, and 46% are extensively annealed. In the "Irumide" age group, 18% of grains are crystalline, 32% are partially annealed, and 50% are extensively annealed. In the oldest group, crystalline and partially annealed zircons represent 14% of the population each, and 72% are extensively annealed.

Sample NH45 has similar age populations with similar proportions of crystalline and metamict zircons as sample NH10 (<0.7 Ga, 44%; 0.7-1.5 Ga, 51%; >1.5 Ga, 5%). In the young group, 41%

of zircon grains are crystalline (*trend 1*), 33% are partially annealed (*trend 2*), and 26% are extensively annealed (*trend 3*). In the intermediate age group, only 10% of grains are crystalline, 61% are partially annealed, and 29% are extensively annealed. In the old group, crystalline zircons are lacking, 67% of grains are partially annealed, and 33% are extensively annealed. Data indicate an increase of extensively annealed zircons in the oldest populations, whereas young zircons (Panafrican in age, or younger) were less affected by thermal annealing.

6.4. Identification of the annealing events

Each zircon grain plotting to the right of the expected trend between Raman peak position and accumulated α-damage indicates thermal annealing (Figs. 1 and 7A). If the age of major thermal events associated with either igneous activity or orogenic metamorphism in potential source rocks is known, then these ages can be used to calculate the α-doses (equation 1) accumulated after those thermal events that may have restored the zircon crystalline structure damaged by α-decay since crystallisation. If the thermal history of source areas is poorly constrained, or in ancient settings where source terranes have been entirely eroded, then the age of the main thermal events can be infer to correspond to the main age peaks obtained by U-Pb dating.

The newly calculated α-doses based on the estimated age of the thermal event are lower than those for the original crystallization, and reflect the damage accumulated after the annealing event (Nasdala et al., 2001). By iteratively calculating the α-doses accumulated since each potential thermal event, each zircon grain is thus progressively shifted to the left in an α-dose *vs*. $\nu_3(SiO_4)$-Raman-peak position diagram for younger and younger thermal events, until the expected trend is reached (Fig. 8). In this way, we can assess for each grain which is the most likely age of the last major thermal-annealing event. Such an age would be generally older than the stratigraphic age of the sample. Annealing occurring after deposition within the sedimentary basin rather than in the

source area is inferred when all zircons display annealing ages that are younger than the age of the sediment. Alternatively, individual zircon grains that plot along *trends 2* or *3* even when accumulated damage has been calculated using the age of the youngest annealing event might be expected if the analysed grains underwent multiple annealing events. In this latter case, each event contributed to restore the crystallinity in spite of the continuous increase of α-doses since original crystallization. This effect will cause the $\nu_3(SiO_4)$-Raman-peak position to be notably higher than expected from the accumulated doses, thus leading to postulate very young annealing ages that may not correspond with actual thermal events. This is because the α-dose would need to be reduced considerably (i.e. calculated using a very young age in equation 1) to restore a normal $\nu_3(SiO_4)$-Raman-peak position/accumulated dose ratios (i.e. along *trend 1*).

In our African case study, the main thermal events to be considered took place around ~ 1.0 Ga (Irumide orogeny; De Waele et al., 2009), ~ 0.6 Ga (Pan-African orogeny; Fritz et al., 2013), 280-180 Ga (Permian to Early Jurassic Karoo igneous events; Jourdan et al., 2006; Daszinnies et al., 2009), and ~120 Ma (Mozambique basin magmatism; König and Jokat, 2010). Therefore, for each zircon grain plotting outside of the expected trend between Raman peak position and accumulated α-damage (i.e. *trends 2* and *3* in Fig. 7C, 7D, 7E) we calculated a new α-dose according to *equation 1*, using 1.0, 0.6, 0.26, and 0.12 Ga. as approximate ages of these thermal events. Uncertainties in Raman data, U-Th concentrations, and age of the thermal events were considered by calculating an α-dose corresponding to the given age of the thermal event ± 10%. The age of the last thermal event can be inferred as the age corresponding to the α-dose for which each zircon plots closest to *trend 1* (Fig. 8).

6.5. Assessing the effect of annealing events

Annealing of metamict zircons affects the relationship between Raman peak position and radiation dose, because the $\nu_3(SiO_4)$-Raman-peak position is shifted toward the crystalline value of 1008 cm^{-1} independently of the radiation dose accumulated since crystallization (Fig. 7B). Unannealed zircon grains display highest Δpeak/dose values, where Δpeak indicates the difference between a $\nu_3(SiO_4)$-Raman-peak position of 1008 cm^{-1} (crystalline zircon) and the actual peak position. Annealed zircons have higher crystallinity than expected from their age and actinide content. They should thus display a lower Δpeak/dose ratio, which is closer to that of unannealed grains for older thermal events (because they have been accumulating damage for a longer time since annealing) and becomes progressively lower for younger thermal events. By means of a U-Pb age *vs*. Δpeak/dose plot we can thus evaluate the impact of the thermal events identified for each annealed zircon grain (following the approach described in section 6.4) on the different age populations of detrital zircons (Fig. 9). For the same annealing event, older zircon grains show lower Δpeak/dose ratios, because of the higher doses accumulated since crystallization leading to incomplete annealing. Twenty-five grains (9% of the entire dataset), mostly displaying extensive annealing (*trend 3*), plot very low along the Δpeak/dose axis, indicating "extreme" crystallinity with respect to the accumulated dose. For these grains, the youngest thermal event (Cretaceous in age) was found to be insufficient to restore their peak position vs. dose relationship to normal values (*trend 1*). As the depositional age of sample NH10 post-dates the Early Cretaceous volcanic activity in the Mozambique channel, the occurrence of younger thermal events is ruled out, as well as annealing during burial after deposition, because all zircons would be affected by such event. The easiest explanation for such extremely high Δpeak/dose ratios is that these grains were involved in multiple annealing events, each of them contributing to increase their cristallinity.

The described method works well only when both Raman and LA-ICP-MS analyses are performed on the same crystal domain. If this requirement is not met, then potential problems may arise in the data interpretation. For instance, one zircon grain in sample NH27 (* in Fig. 9) yields a

crystallization age of 118 Ma and a post-Cretaceous annealing age. Because the young crystallization age of this zircon rules out the effect of multiple annealing events, it should be either older or less crystalline to fit in our scheme. Its anomalous $\nu_3(SiO_4)$-Raman-peak position vs. α-dose relationship thus suggests that Raman and U/Pb spots have targeted different domains within the same zircon grain.

7. Improving provenance discriminations

U-Pb age spectra of detrital zircons contained in the three studied samples allow discrimination of four main primary provenances: Archean-Paleoproterozoic terranes, the Irumide orogen, the Pan-African orogen, and Lower Cretaceous volcanic rocks. Considering that zircon-bearing magmatic or metamorphic rocks of ~1 Ga or ~0.6 Ga occur throughout the Irumide and Pan-African belts widely exposed across southern Africa from Namibia to Mozambique and from Zimbabwe to Zambia, and that zircon grains can be recycled from siliciclastic sedimentary rocks an unknown number of times, such a provenance estimation is too vague to help us to pin-point actual sediment sources univocally. A more accurate identification of the potential sources and dispersal paths of zircon grains can be achieved by combining U-Pb dating with Raman spectroscopy, allowing us to distinguish four to five different subpopulations of similarly aged grains with different thermal histories (Fig. 10).

In the Valanginian/Hauterivian sample NH45, partially annealed *trend 2* zircons mostly represent Irumide ages that were affected by both Pan-African and Karoo thermal events, whereas those yielding Pan-African ages recorded Late Permian and Early Jurassic events. Source areas most likely located south of Lake Malawi are suggested for most of these partially annealed grains based on the present distribution of rocks matching such a complex geological evolution (Fig. 2). Most Irumide and Pan-African *trend 3* zircons record a complex, possibly multi-phased annealing history (Fig. 10), as the youngest known annealing event (Early Cretaceous) is insufficient to restore a

normal dose/peak ratio. The occurrence of unannealed zircons (*trend 1*) limits the chances of post-depositional annealing during burial.

A drastic provenance change is documented by the Aptian/Albian sample NH27, where many zircons yielded Early Cretaceous ages and were thus generated from penecontemporaneous volcanism in coastal Mozambique. These zircons show no sign of subsequent annealing. Partially annealed *trend 2* zircons of both Irumide and Pan-African-ages were largely affected by the Late Permian event. Among *trend 3* zircons, a few grains with the oldest U-Pb ages were finally annealed in the Late Permian, several Irumide-aged zircons in the Early Jurassic and Early Cretaceous, and Pan-African-aged zircons show a complex history.

In the Cenomanian/Turonian sample NH10, zircon populations are remarkably similar as those in sample NH45, with a more extensive Pan-African effect on partially annealed *trend 2* Irumide-aged zircons. The Early Cretaceous thermal event, lacking in the oldest sample NH45, is recorded by ~10% of the analysed zircons in sample NH10. *Trend 3* zircons of Pan-African age were affected by the Early Cretaceous thermal event, or were involved in multiple annealing stages, whereas Irumide-aged *trend 3* zircons also display annealing during Permian and Jurassic.

8. **Conclusions**

The innovative combination of Raman spectroscopy with classic LA-ICP-MS U-Pb dating on the same zircon grains leads to a sharp improvement of resolution power in provenance analysis of detrital zircon. The $\nu_3(SiO_4)$ Raman peak of zircon crystals broadens and shifts to a lower position with increasing metamict state. These features allow us not only to discriminate among zircon grains with different metamict state and different degrees of annealing but also to estimate a geologically viable age for the annealing event. Identifying different zircon subpopulations with the same crystallization age but different subsequent thermal histories adds further cogent constraints that allow us to discriminate among different potential source terranes with similar ages of crustal

growth and thus to pinpoint detrital sources considerably reducing ambiguities and improving provenance diagnoses.

ACKNOWLEDGMENTS

The studied samples were provided by Total E&P oil company in the frame of a source-to-sink study joint with the Laboratory of Provenance Studies of the University of Milano-Bicocca on the Cretaceous-Cenozoic evolution of the Zambezi Delta Lorenzo Pirovano contributed to this study during his Master Thesis. Careful reviews by Heinrich Bahlburg and an anonymous reviewer are gratefully acknowledged.

SUPPLEMENTARY MATERIAL

The geochemical and geochronological data and the calculated alpha-decay dose for each zircon grain is provided in Appendix Table A1.

REFERENCES CITED:

Balan, E., Neuville, D.R., Trocellier, P., Fritsch, E., Muller, J.P. and Calas, G., 2001. Metamictization and chemical durability of detrital zircon. American Mineralogist, 86(9), 1025-1033.

Brøgger, W.C., 1896. Amorf: Salmonsens store illustrerede Konversations-Lexikon, v. 1. Abstract in Zeit. Kryst, 16, pp.427-428.

Catuneanu, O., Wopfner, H., Eriksson, P.G., Cairncross, B., Rubidge, B.S., Smith, R.M.H., Hancox, P.J., 2005. The Karoo basins of south-central Africa. Journal of African Earth Sciences, 43(1-3), 211-253.

Chakoumakos, B.C., Murakami, T., Lumpkin, G.R., Ewing, R.C., 1987. Alpha-decay—Induced fracturing in zircon: The transition from the crystalline to the metamict state. Science, 236(4808), 1556-1559.

Condie, K.C., Belousova, E., Griffin, W.L., Sircombe, K.N., 2009. Granitoid events in space and time: constraints from igneous and detrital zircon age spectra. Gondwana Research, 15(3-4), 228-242.

Condon, D. J., Schoene, B., McLean, N. M., Bowring, S. A., Parrish, R. R., 2015. Metrology and traceability of U–Pb isotope dilution geochronology (EARTHTIME Tracer Calibration Part I). *Geochimica et Cosmochimica Acta*, *164*, 464-480.

Daszinnies, M.C., Jacobs, J., Wartho, J.A. and Grantham, G.H., 2009. Post Pan-African thermo-tectonic evolution of the north Mozambican basement and its implication for the Gondwana rifting. Inferences from 40Ar/39Ar hornblende, biotite and titanite fission-track dating. Geological Society, London, Special Publications, 324(1), pp.261-286.

Dawson, P., Hargreave, M.M. and Wilkinson, G.R., 1971. The vibrational spectrum of zircon (ZrSiO4). Journal of Physics C: Solid State Physics, 4(2), 240-256.

De Waele, B., Kampunzu, A.B., Mapani, B.S.E., Tembo, F., 2006. The Mesoproterozoic Irumide belt of Zambia. Journal of African Earth Sciences, 46(1-2), 36-70.

De Waele, B., Fitzsimons, I.C.W., Wingate, M.T.D., Tembo, F., Mapani, B., Belousova, E.A., 2009. The geochronological framework of the Irumide Belt: a prolonged crustal history along the margin of the Bangweulu Craton. American Journal of Science, 309(2), 132-187.

Ewing, R.C., Haaker, R.F., Lutze, W., 1982. Leachability of zircon as a function of alpha dose. Scientific Basis for Radioactive Waste Management, 5, 389–397.

Ewing, R.C., Chakoumakos, B.C., Lumpkin, G.R., Murakami, T., 1987. The metamict state. Material Research Society Bulletin, 12(4), 58-66.

Farley, K.A., 2002. (U-Th)/He-dating: Techniques, calibrations, and applications. Reviews in

Mineralogy and Geochemistry, 47(1), 819-844.

Fedo, C.M., Sircombe, K.N., Rainbird, R.H., 2003. Detrital zircon analysis of the sedimentary record. Reviews in Mineralogy and Geochemistry, 53(1), 277-303.

Fritz, H., Abdelsalam, M., Ali, K.A., Bingen, B., Collins, A.S., Fowler, A.R., Ghebreab, W., Hauzenberger, C.A., Johnson, P.R., Kusky, T.M., Macey, P., 2013. Orogen styles in the East African Orogen: a review of the Neoproterozoic to Cambrian tectonic evolution. Journal of African Earth Sciences, 86, 65-106.

Garzanti, E., Vermeesch, P., Vezzoli, G., Andò, S., Botti, E., Limonta, M., Dinis, P., Hah, A., Baudet, D., De Grave, J., Yaya, N.K., 2019. Congo River sand and the equatorial quartz factory. Earth-Science Reviews, 102918. doi/10.1016/j.earscirev.2019.102918.

Gehrels, G., 2011. Detrital zircon U-Pb geochronology: Current methods and new opportunities. Tectonics of sedimentary basins: Recent advances, 45-62.

Geisler, T., 2002. Isothermal annealing of partially metamict zircon: evidence for a three-stage recovery process. Physics and Chemistry of Minerals, 29(6), pp.420-429.

Ginster, U., Reiners, P.W., Nasdala, L., Chanmuang N. C., 2019. Annealing kinetics of radiation damage in zircon. Geochimica et Cosmochimica Acta, 249, 225-246.

Glynn, S.M., Master, S., Wiedenbeck, M., Davis, D.W., Kramers, J.D., Belyanin, G.A., Frei, D., Oberthür, T., 2017. The Proterozoic Choma-Kalomo Block, SE Zambia: Exotic terrane or a reworked segment of the Zimbabwe Craton? Precambrian Research, 298, 421-438.

Goscombe, B., Foster, D.A., Gray, D., Wade, B., 2019. Assembly of central Gondwana along the Zambezi Belt: Metamorphic response and basement reactivation during the Kuunga Orogeny. Gondwana Research, doi.org/10.1016/j.gr.2019.11.004

Griffin, W.L., Powell, W.J., Pearson, N.J., O'Reilly, S.Y., 2008. GLITTER: Data reduction software for laser ablation ICP-MS. In: Sylvester, P. (ed.), Laser Ablation-ICP-MS in the Earth Sciences: Current Practices and Outstanding Issues. Mineralogical Association of Canada, Short Course, Series 40, 204–207.

Haddon, I.G., McCarthy, T.S., 2005. The Mesozoic–Cenozoic interior sag basins of Central Africa: The Late-Cretaceous–Cenozoic Kalahari and Okavango basins. J. Afr. Earth Sci., 43, 316-333.

Hanson, R.E. 2003. Proterozoic geochronology and tectonic evolution of southern Africa. In Yoshida, M.; Windley, B.F.; and Dasgupta, S. (eds.), Proterozoic East Gondwana: supercontinent assembly and breakup. Geol. Soc. London, Spec. Publ. 206, 427-463.

Hanson, R.E., Harmer, R.E., Blenkinsop, T.G., Bullen, D.S., Dalziel, I.W.D., Gose, W.A., Hall, R.P., Kampunzu, A.B., Key, R.M., Mukwakwami, J., Munyanyiwa, H., Pancake, J.A., Seidel,

E.K., Ward, S.E., 2006. Mesoproterozoic intraplate magmatism in the Kalahari Craton: a review. J. Afr. Earth Sci., 46, 141-167.

Hargrove, U.S., Hanson, R.E., Martin, M.W., Blenkinsop, T.G., Bowring, S.A., Walker, N. and Munyanyiwa, H., 2003. Tectonic evolution of the Zambezi orogenic belt: geochronological, structural, and petrological constraints from northern Zimbabwe. Precambrian Research, 123(2-4), pp.159-186.

Holland, H.D., Gottfried, D., 1955. The effect of nuclear radiation on the structure of zircon. Acta Crystallographica, 8, 291-300.

Hoskin, P.W.O., Ireland, T.R., 2000. Rare earth element chemistry of zircon and its use as a provenance indicator. Geology, 28 (7), 627-630.

Hurford, A.J., Carter, A., 1991. The role of fission track dating in discrimination of provenance. Geological Society, London, Special Publications, 57(1), 67-78Isozaki, Y., Yamamoto, S., Sakata, S., Obayashi, H., Hirata, T., Obori, K.-I., Maebayashi, T., Takeshima, S., Ebisuzaki, T., Maruyama, S., 2018. High-reliability zircon separation for hunting the oldest material on Earth: An automatic zircon separator with image-processing/microtweezers-manipulating system and double-step dating. Geoscience Frontiers, 9 (4), 1073-1083.

Hurley, P.M., Fairbairn, H.W., 1953. Radiation damage in zircon: a possible age method. Geological Society of America Bulletin, 64(6), 659-673.

Jackson, S.E., Pearson, N.J., Griffin, W.L., Belousova, E.A., 2004. The application of laser ablation-inductively coupled plasma-mass spectrometry to in situ U–Pb zircon geochronology. Chem. Geol. 211, 47–69.

Jacobs, J., Pisarevsky, S., Thomas, R.J., Becker, T. 2008. The Kalahari Craton during the assembly and dispersal of Rodinia. Precambrian Res., 160, 142-158.

Jelsma, H.A., Dirks, P.H.G.M., 2002. Neoarchaean tectonic evolution of the Zimbabwe Craton. *In* Fowler, C.M.R.; Ebinger, C.J.: and Hawkesworth, C.J. (eds.), The early Earth: physical, chemical and biological development. Geol. Soc. London, Spec. Publ. 199, 183-211.

Johnson, M.R., Van Vuuren, C.J., Hegenberger, W.F., Key, R., Show, U., 1996. Stratigraphy of the Karoo Supergroup in southern Africa: an overview. Journal of African Earth Sciences, 23(1), 3-15.

Jourdan, F., Féraud, G., Bertrand, H., Watkeys, M.K., Kampunzu, A.B., Le Gall, B., 2006. Basement control on dyke distribution in Large Igneous Provinces: case study of the Karoo triple junction. Earth and Planetary Science Letters, 241(1-2), 307-322.

Kemp, A.I.S., Hawkesworth, C.J., Paterson, B.A., Kinny, P.D., 2006. Episodic growth of the Gondwana supercontinent from hafnium and oxygen isotopes in zircon. Nature, 439(7076),

580-583.

König, M., Jokat, W., 2010. Advanced insights into magmatism and volcanism of the Mozambique Ridge and Mozambique Basin in the view of new potential field data. Geophysical Journal International, 180(1), 158-180.

Malusà, M.G., Carter, A., Limoncelli, M., Villa, I.M., Garzanti, E., 2013. Bias in detrital zircon geochronology and thermochronometry. Chemical Geology, 359, 90-107.

Mezger, K., Krogstad, E.J., 1997. Interpretation of discordant U-Pb zircon ages: An evaluation. Journal of metamorphic Geology, 15(1), 127-140.

Murakami, T., Chakoumakos, B.C., Ewing, R.C., Lumpkin, G.R., Weber, W.J., 1991. Alpha-decay event damage in zircon. American Mineralogist, 76(9-10), 1510-1532.

Nasdala, L., Pidgeon, R.T., Wolf, D., Irmer, G., 1998. Metamictization and U-Pb isotopic discordance in single zircons: a combined Raman microprobe and SHRIMP ion probe study. Mineralogy and Petrology, 62(1-2), 1-27.

Nasdala, L., Wenzel, M., Vavra, G., Irmer, G., Wenzel, T., Kober, B., 2001. Metamictisation of natural zircon: accumulation versus thermal annealing of radioactivity-induced damage. Contributions to Mineralogy and Petrology, 141(2), 125-144.

O'Haver, T., 2020. A Pragmatic Introduction to Signal Processing with applications in scientific measurement: An illustrated book with free software and spreadsheet templates to download. ISBN: 9798611266687, https://terpconnect.umd.edu/~toh/spectrum/TOC.html.

Pupin, J.P., 1980. Zircon and granite petrology. Contributions to Mineralogy and Petrology, 73(3), 207-220.

Salman, G., Abdula, I., 1995. Development of the Mozambique and Ruvuma sedimentary basins, offshore Mozambique. Sedimentary Geology, 96, 7-41.

Sláma, J., Košler, J., Condon, D.J., Crowley, J.L., Gerdes, A., Hanchar, J.M., Horstwood, M.S., Morris, G.A., Nasdala, L., Norberg, N., Schaltegger, U., 2008. Plešovice zircon — a new natural reference material for U–Pb and Hf isotopic microanalysis. Chem. Geol. 249, 1–35.

Svensen, H., Corfu, F., Polteau, S., Hammer, Ø., Planke, S. 2012. Rapid magma emplacement in the Karoo Large Igneous Province. Earth Planet. Sci. Lett., 325/326, 1-9.

Velbel, M.A., 1999. Bond strength and the relative weathering rates of simple orthosilicates. Am. J. Sci. 299, 679–696.

Vermeesch, P., Garzanti, E., 2015. Making geological sense of 'Big Data'in sedimentary provenance analysis. Chemical Geology, 409, 20-27.

Vermeesch, P., Resentini, A., Garzanti, E., 2016. An R package for statistical provenance analysis. Sedimentary Geology, 336, 14-25.

Vermeesch, P., Rittner, M., Petrou, E., Omma, J., Mattinson, C., Garzanti, E., 2017. High throughput petrochronology and sedimentary provenance analysis by automated phase mapping and LAICPMS. Geochemistry, Geophysics, Geosystems, 18(11), 4096-4109.

Weber, W.J., Ewing, R.C., Wang, L.M., 1994. The radiation-induced crystalline-to-amorphous transition in zircon. Journal of Materials Research, 9(3), 688-698.

Zhang, M., Salje, E.K., Capitani, G.C., Leroux, H., Clark, A.M., Schlüter, J., Ewing, R.C., 2000. Annealing of-decay damage in zircon: a Raman spectroscopic study. Journal of Physics: Condensed Matter, 12(13), 3131–3148.

Zimmermann, S., Mark, C., Chew, D., Voice, P.J., 2018. Maximising data and precision from detrital zircon U-Pb analysis by LA-ICPMS: The use of core-rim ages and the single-analysis concordia age. Sedimentary Geology, 375, 5-13.

FIGURE CAPTIONS

Figure 1. Progressive degree of metamictization as revealed by Raman spectroscopy in zircon crystals with complete accumulation of radiation damage. **Upper panel**) Increasing full width at half maximum (FWHM) of the $\nu_3(SiO_4)$ Raman peak with damage accumulation (data after Nasdala et al., 2001). **Lower panel**) Shifting position of the $\nu_3(SiO_4)$ Raman peak with damage accumulation (FWHM data after Nasdala et al., 2001, converted using *equation* 2).

Figure 2. Sketch geological and geochronological map of Mozambique, Malawi, and Zambia (after Hanson, 2003, DeWaele et al., 2006, Jourdan et al., 2006 and Goscombe et al., 2019). Different terranes with age of crustal growth ranging widely from Archean to Cambrian were affected by diverse younger stages of thermal overprint, the most intense of which took place during the Neoproterozoic Pan-African orogeny.

Figure 3. Deconvolution of Raman peaks in one zircon grain from sample NH10. Peak position and full width at half maximum (FWHM) are indicated.

Figure 4. U-Pb age-spectra of detrital zircons in samples NH45, NH27 and NH10 (age *vs*. frequencies plotted as Kernel Density Estimates using the *provenance* package of Vermeesch et al., 2016).

Figure 5. Inverse correlation between position and full width at half maximum of the $\nu_3(SiO_4)$ Raman peak (R^2 0.80). A narrow peak at ~1008 cm^{-1} is diagnostic of fully crystalline grains, whereas lower positions and wider peaks indicate a progressive degree of metamictization (Nasdala et al., 1998).

Figure 6. Relationships of zircon U-Pb ages with accumulated α-dose and $\nu_3(SiO_4)$ Raman peak. The lack of strongly metamict old zircon grains suggests lower chemical and/or mechanical durability and hence selective loss during repeated sedimentary cycles.

Figure 7. Identifying different thermal histories of detrital zircons. **A**) Complex relationship between accumulated radiation dose and $\nu_3(SiO_4)$ Raman peak position. The grey area represents the field of nearly complete accumulation of damage calculated from zircons reported in Nasdala et al. (2001). **B**) Definition of the three annealing trends by plotting the downshift of the Raman peak relative to 1008 cm^{-1} *versus* radiation dose for each zircon grain. **C, D. E**) Partitioning among *trends 1*, *2* and *3* of zircon grains in samples NH10, NH27, and NH45.

Figure 8. Identification of the annealing event. For each zircon, the $\nu_3(SiO_4)$ Raman peak position/accumulated α-dose should lie on *trend 1* (white square). If the calculated α-dose (grey square) is greater than that expected following *trend 1* (complete accumulation of damage) for the measured position of the $\nu_3(SiO_4)$ Raman peak, the zircon grain was thermally annealed.

We can estimate the age for which the accumulated α-damage would match the crystallinity of the zircon with a trial and error approach. By using the ages of potential annealing events known for inferred source areas, we recalculate the accumulated α-damage from the age of each thermal event (coloured circles). Accumulated α-doses will be lower and lower for younger and younger thermal events, until *trend 1* is eventually reached. The oldest event, whose age restores the normal $\nu_3(SiO_4)$ Raman peak position *vs* radiation dose ratio (*trend 1*), is taken as the age of annealing.

Figure 9. Discriminating subpopulations of detrital zircons with same crystallization age (determined by U-Pb geochronology) but different annealing history (determined by Raman spectroscopy). Nearly one third of the analysed zircon grains show no thermal annealing. The

Karoo event is estimated to have affected > 25% of analysed grains, resulting to be a major thermal event, whereas fewer grains recorded Jurassic, Early Cretaceous or Pan-African heating. About 7% of zircon grains yielded low Δpeak/dose ratio, indicating very recent annealing or, more probably, multiple annealing events through time. Note that all zircons older than 1.3 Ga underwent thermal annealing. The zircon grain from sample NH27 denoted with the symbol * is anomalous: it should either have a greater Δpeak/dose ratio (unannealed zircon) or should yield an older age.

Figure 10. Provenance discrimination of detrital zircons improved. Several subpopulations of zircon grains with similar age but different thermal histories can be distinguished by combining U-Pb dating and analysis of the position of the $\nu_3(SiO_4)$ Raman peak. For each sample, the relative proportions of grain-age populations based on U-Pb age (thick bar), crystallinity (intermediate bar), and age of annealing events (thin bar) are given. Note that the combined-age fingerprints of samples NH45 and NH10 are similar, and distinct from those of sample NH27. When the age of the annealing event is taken into account, the Karoo thermal event affected most zircons in sample NH45, whereas Cretaceous heating characterizes annealed zircons in sample NH10.

Figure 1

Click here to download high resolution image

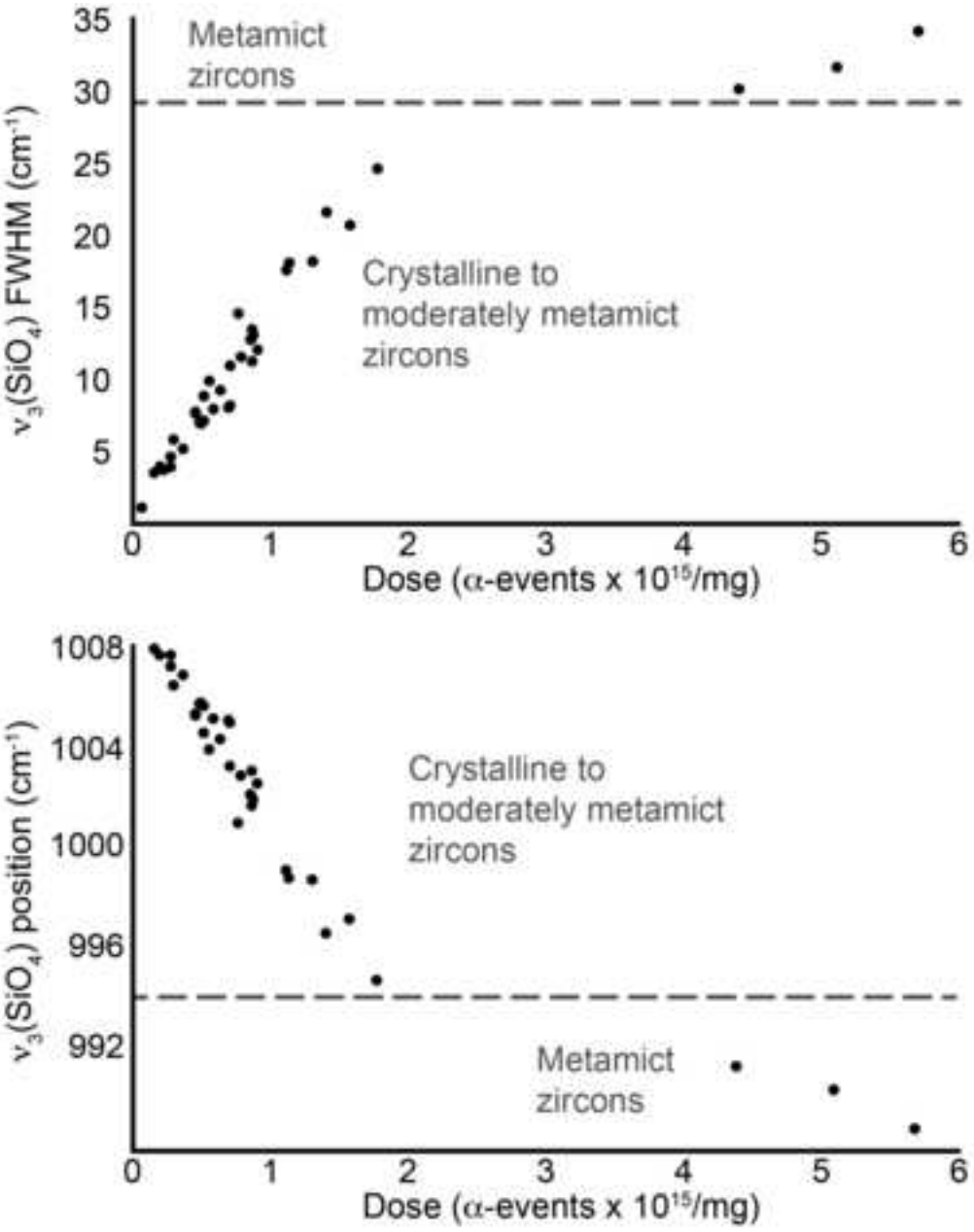

Figure 2

Click here to download high resolution image

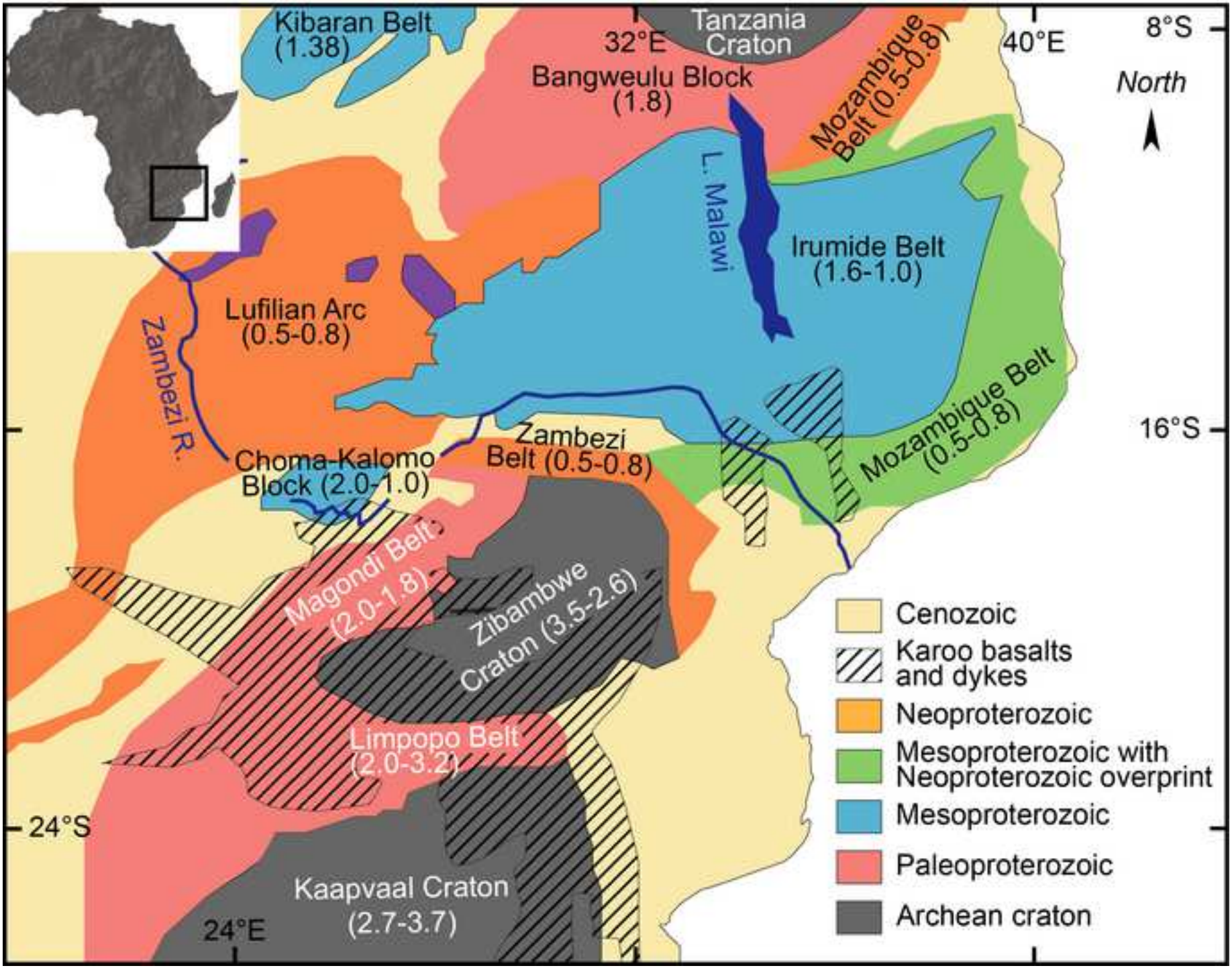

Figure 3

Click here to download high resolution image

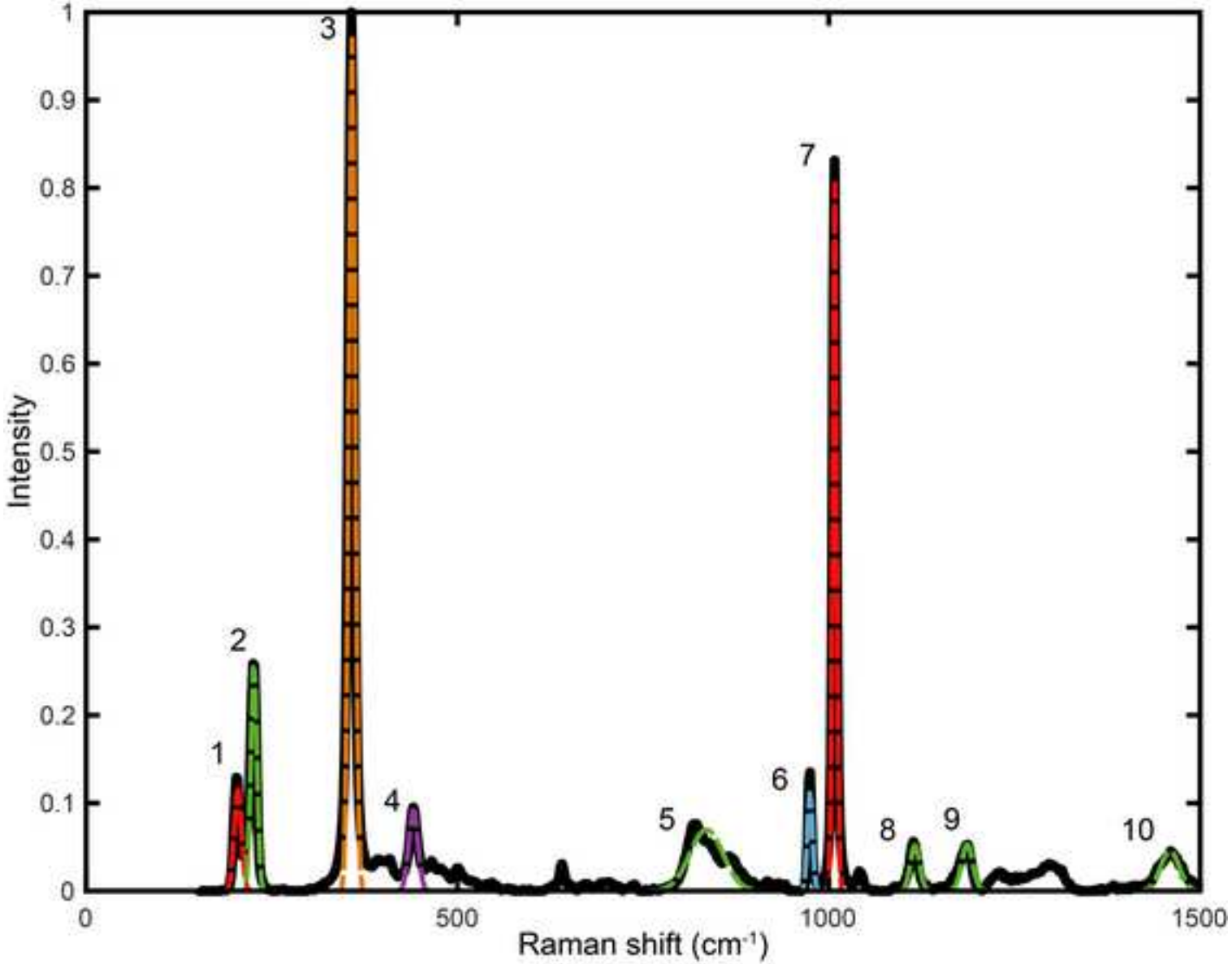

Peak	1	2	3	4	5	6	7	8	9	10
Position *(cm⁻¹)*	203.5	225.1	357	441.4	833.2	974.3	1008	1114	1184	1473
FWMH *(cm⁻¹)*	11.65	9.66	9.84	14.39	52.52	8.14	6.32	14.67	17.9	10.36

Figure 4

Click here to download high resolution image

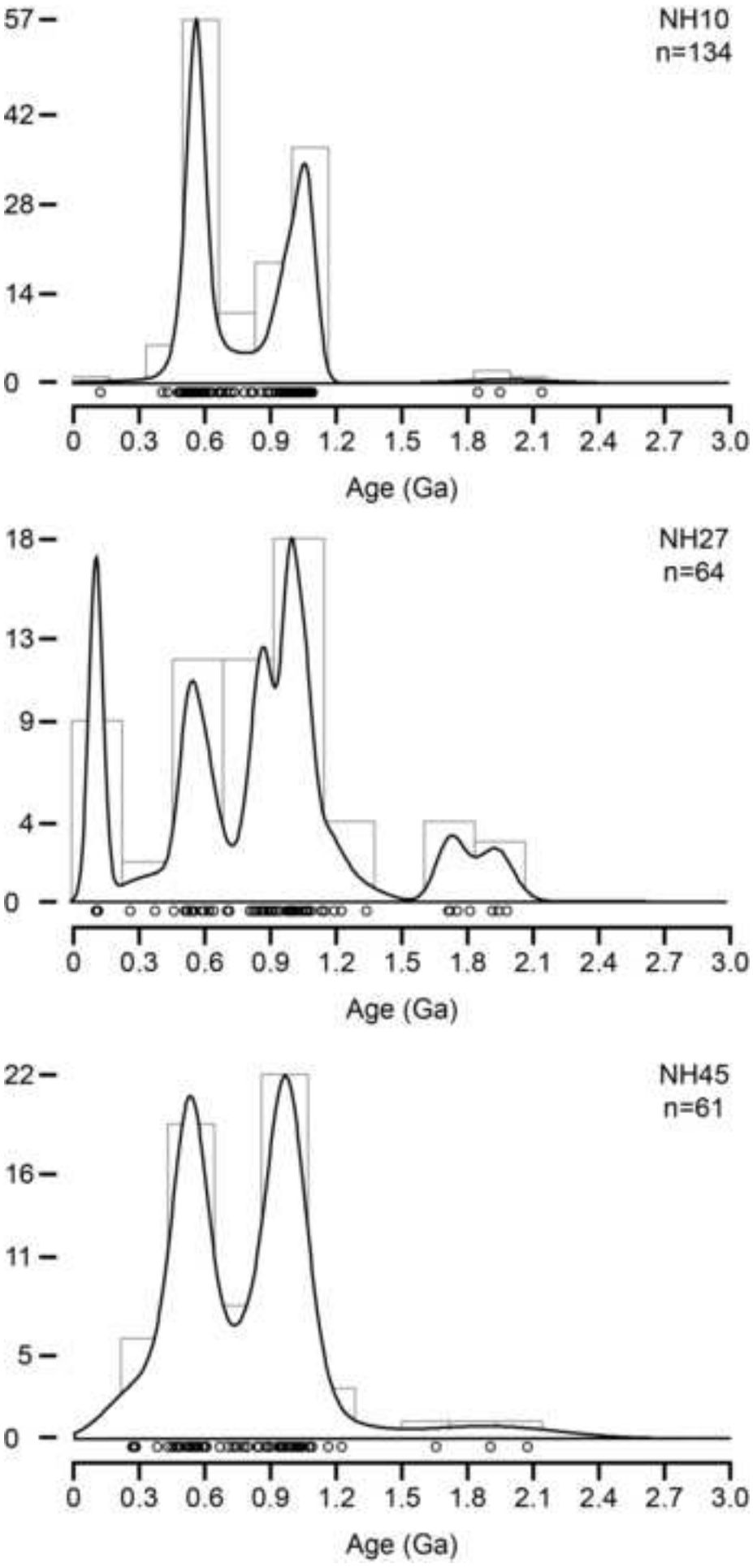

Figure 5

Click here to download high resolution image

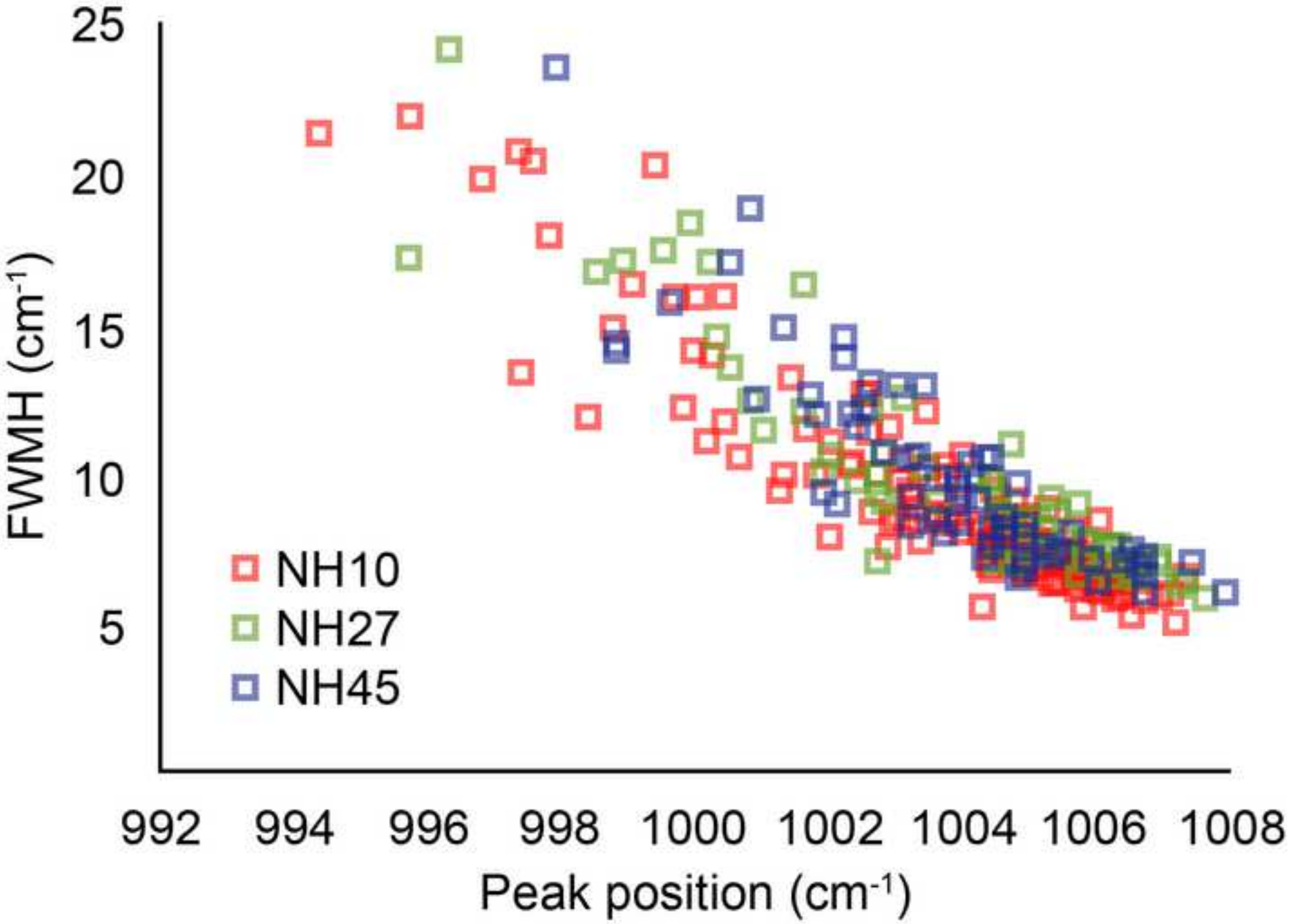

Figure 6
Click here to download high resolution image

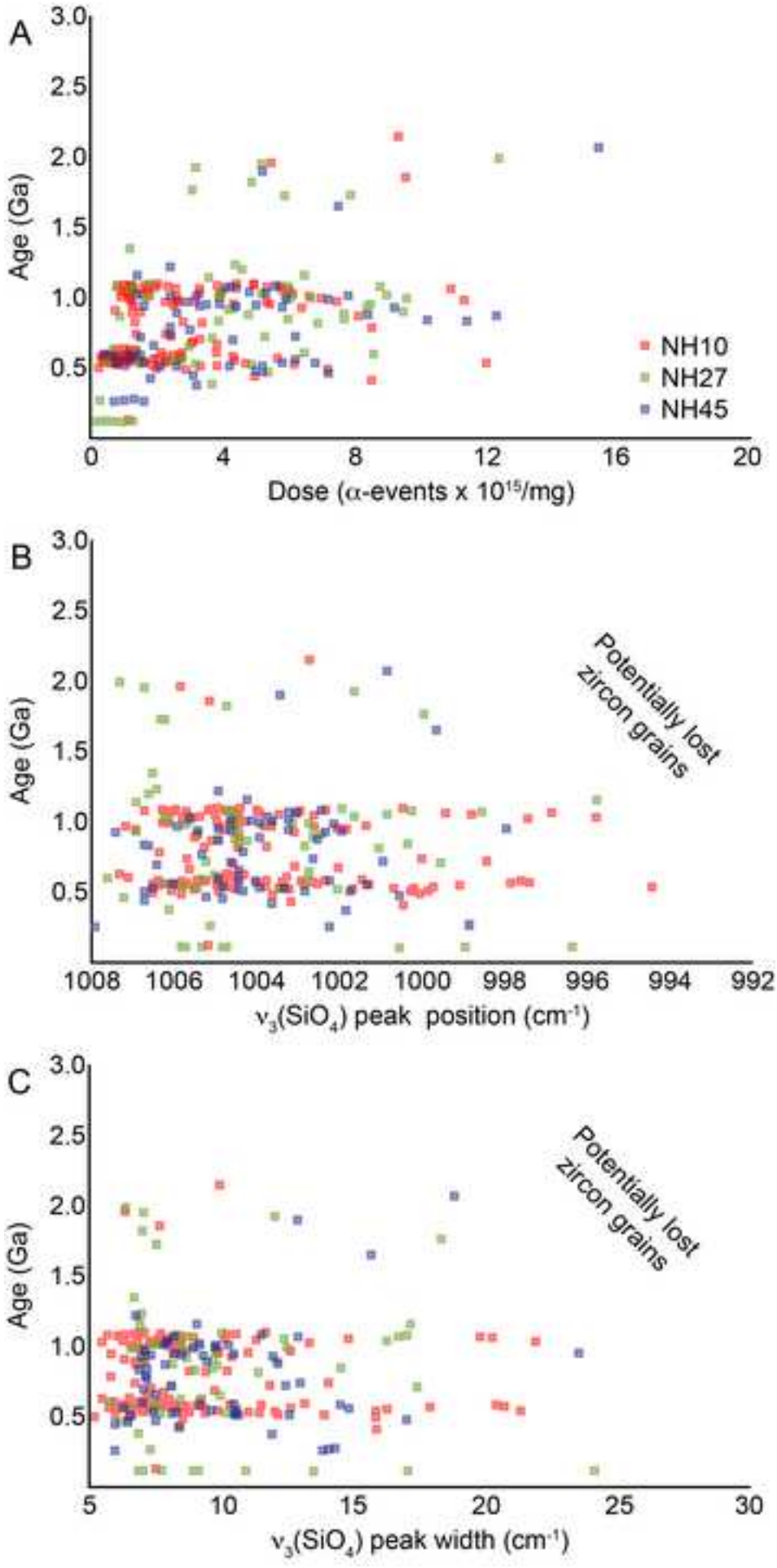

Figure 7

Click here to download high resolution image

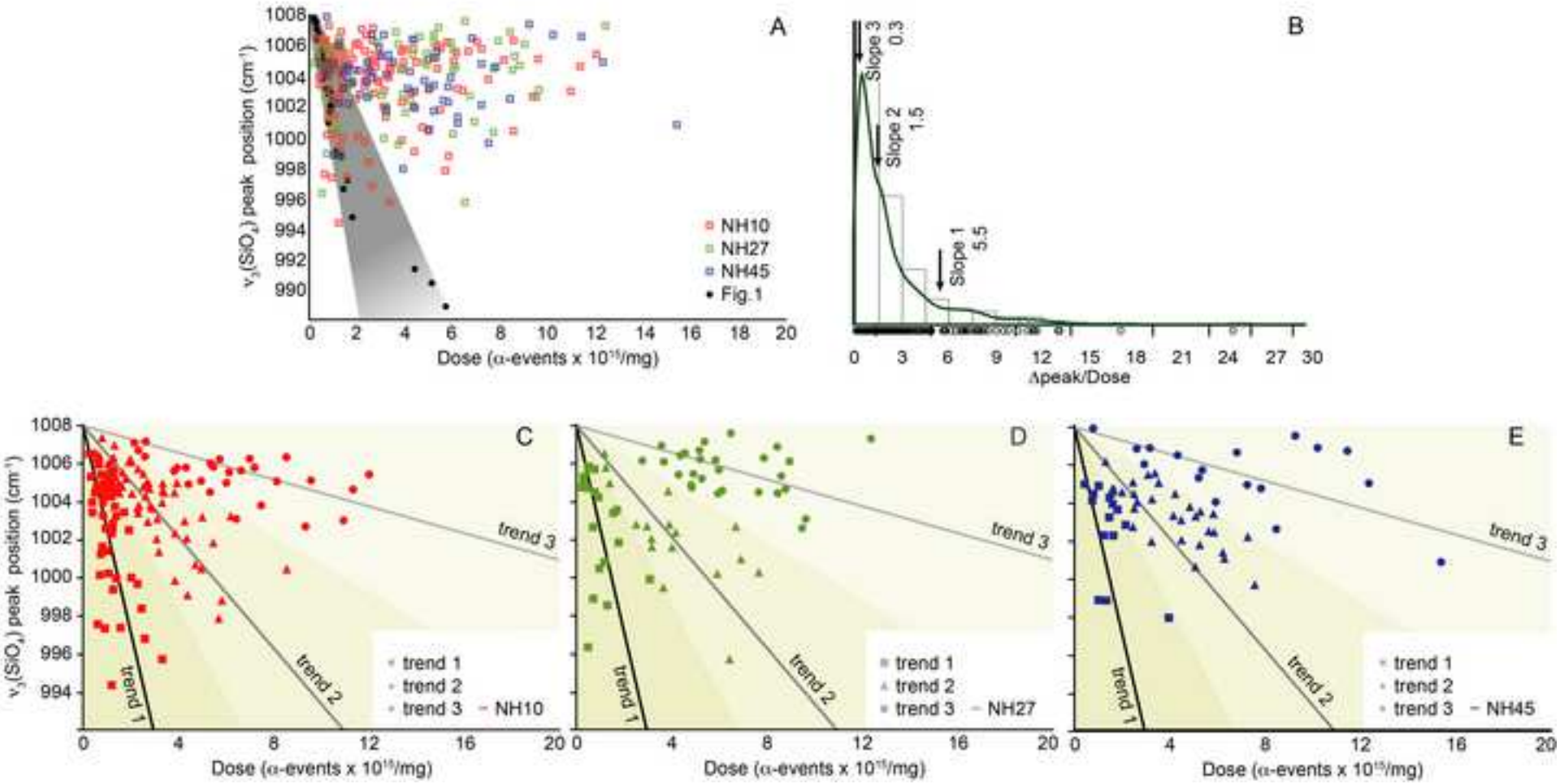

Figure 8

Click here to download high resolution image

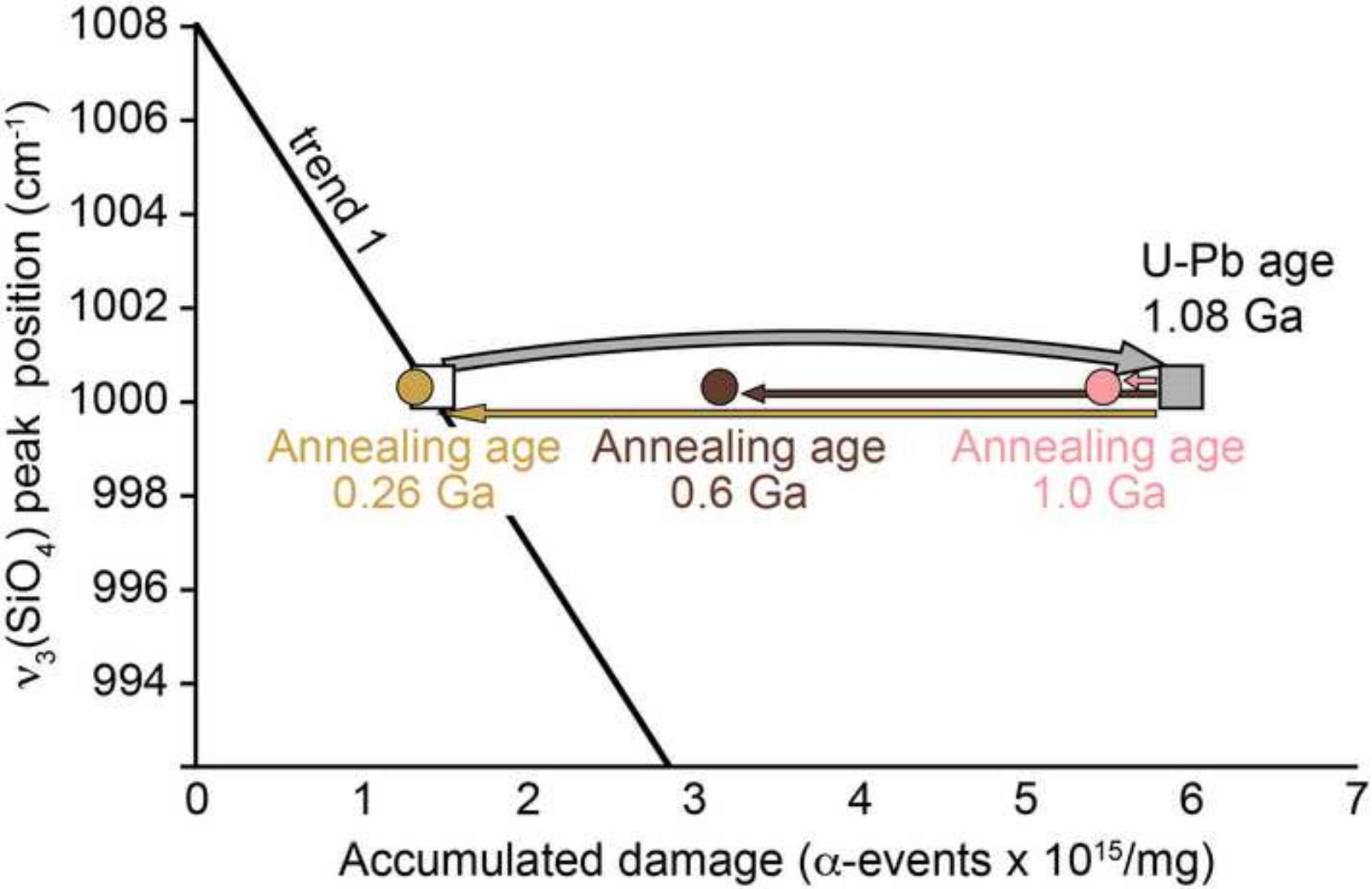

Figure 9
Click here to download high resolution image

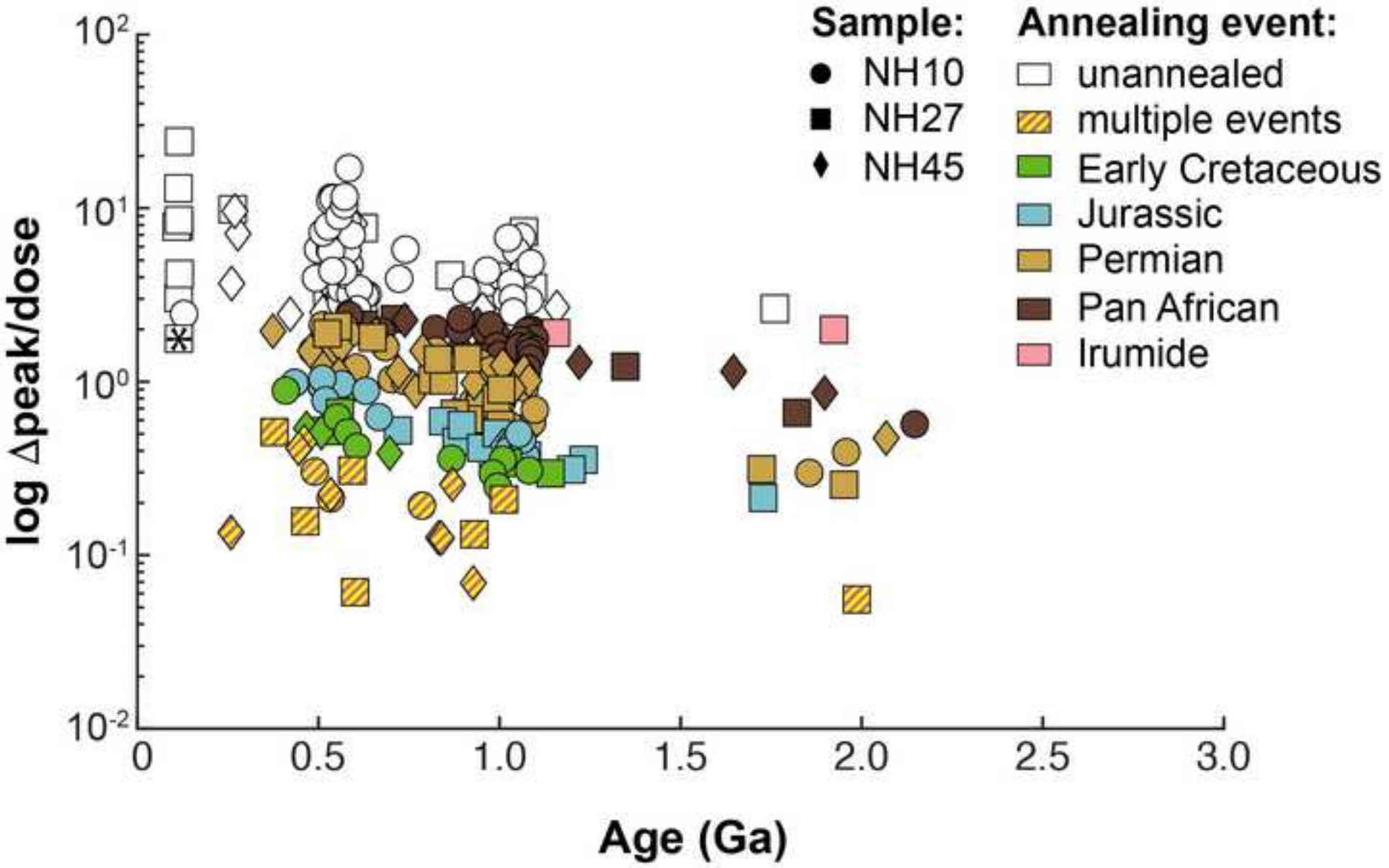

Figure 10
Click here to download high resolution image